ACS APPLIED MATERIALS & INTERFACES

Research Article

Cite This: ACS Appl. Mater. Interfaces XXXX, XXX, XXX−XXX

www.acsami.org

Efficient Type-II Heterojunction Nanorod Sensitized Solar Cells Realized by Controlled Synthesis of Core/Patchy-Shell Structure and CdS Cosensitization

Sangheon Lee,[†] Joseph C. Flanagan,[‡] Jaewook Kim,[†] Alan Jiwan Yun,[†] Byungho Lee,[†] Moonsub Shim,*[,‡] and Byungwoo Park*[,†]

[†]WCU Hybrid Materials Program, Department of Materials Science and Engineering, Research Institute of Advanced Materials, Seoul National University, Seoul 08226, Korea

[‡]Department of Materials Science and Engineering and Frederick Seitz Materials Research Laboratory, University of Illinois at Urbana-Champaign, Urbana, Illinois 61801, United States

Supporting Information

ABSTRACT: Here, we report the successful application of core/patchy-shell CdSe/CdSe$_x$Te$_{1-x}$ type-II heterojunction nanorods (HNRs) to realize efficient sensitized solar cells. The core/patchy-shell structure designed to have a large type-II heterointerface without completely shielding the CdSe core significantly improves photovoltaic performance compared to other HNRs with minimal or full-coverage shells. In addition, cosensitization with CdS grown by successive ionic layer adsorption and reaction further improves the power conversion efficiency. One-diode model analysis reveals that the HNRs having exposed CdSe cores and suitably grown CdS result in significant reduction of series resistance. Investigation of the intercorrelation between diode quality parameters, diode saturation current density (J_0) and recombination order (β = (ideality factor)$^{-1}$) reveals that HNRs with open CdSe cores exhibit reduced recombination. These results confirm that the superior performance of core/patchy-shell HNRs results from their fine-tuned structure: photocurrent is increased by the large type-II heterointerface and recombination is effectively suppressed due to the open CdSe core enabling facile electron extraction. An optimized power conversion efficiency of 5.47% (5.89% with modified electrode configuration) is reported, which is unmatched among photovoltaics utilizing anisotropic colloidal heterostructures as light-harvesting materials.

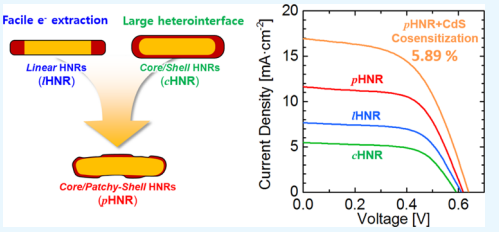

KEYWORDS: *heterojunction nanorod, core/shell, II−VI semiconductor, sensitized solar cell, cosensitization*

INTRODUCTION

Heterojunction nanorods (HNRs), a class of colloidal nanoparticles where semiconductors of differing band gap are adjoined into a one-dimensional rod, offer unprecedented design options in materials for solar energy harvesting and light emitting devices. Compared to "spherical" quantum dots (QDs) that have been more widely studied, HNRs benefit from their elongated geometry, granting them higher intrinsic absorption coefficient,[1] the possibility of enhanced multiple exciton generation,[2,3] and directional manipulation of electron−hole wavefunctions.[4,5] Furthermore, when introduced in HNRs, the type-II heterointerface can serve as a site to efficiently separate photogenerated electron−hole pairs and extend the spectral window of light harvesting by charge-separated state (CSS) absorption.[6,7] In addition to these beneficial features, these types of materials have been successfully integrated into light-emitting diodes (LEDs) recently.[8−11] For example, double-HNRs impart the capability of both emitting and sensing light, allowing the same LED pixel to be used as both a light source and a photodetector.[11]

Despite such benefits and achievements over conventional QDs in LED applications, success of HNRs in photovoltaics has been limited up to now. The most challenging issue in incorporating HNRs as light absorber materials for solar cells originates from their unique morphology, where the electron- and hole-selective components are both exposed to the surface to ensure facile carrier extraction. Increasing thickness of HNR films beyond ∼monolayer to increase absorption leads to the formation of undesired energy barriers, inhibiting carrier transport and limiting the photovoltaic performance of HNR-based prototype photovoltaic devices.[12] We have reported an approach to integrate CdSe/CdSe$_x$Te$_{1-x}$ HNRs into the sensitized solar cell (SSC) architecture, which mitigates this problem by adsorbing a monolayer of HNRs on mesoporous TiO_2 electrodes with large surface area to ensure sufficient light absorption without forming a thick HNR film.[13]

A remaining issue in the HNR-SSC architecture is that using HNRs with a sufficiently large internal heterointerface area desirable for enhancing charge separation and extending the

Received: February 15, 2019
Accepted: May 8, 2019
Published: May 8, 2019

DOI: 10.1021/acsami.9b02873
ACS Appl. Mater. Interfaces XXXX, XXX, XXX−XXX

absorption spectral window can lead to overall reduction in device performance. Core/shell-structured HNRs can be prepared to maximize the near-infrared (NIR) photon harvesting from the type-II heterointerface, but the carrier extraction from the core component becomes prohibited as the core is physically shielded from TiO_2 by the shell with a higher conduction band edge. In our previous report, this complication led to the result of HNRs with the least internal heterointerface area exhibiting the highest power conversion efficiency (PCE) compared to the core/shell-structured HNRs.[14]

In this report, we suggest a solution to this problem. The "core/patchy-shell" CdSe/$CdSe_xTe_{1-x}$ HNRs are successfully synthesized, where an incomplete shell retains the large type-II heterointerface but core CdSe is still exposed to the outside to readily form an electron-selective contact. These HNRs are shown to outperform their counterparts with different shell coverages when incorporated into SSCs. In addition, the effects of CdS cosensitizers grown by the successive ionic layer adsorption and reaction (SILAR) route are systematically investigated to further improve device performance. Cosensitizers have been sparingly explored with colloidal QDs and single-component nanorods.[15−18] Analysis of cosensitized solar cells based on the one-diode model provides valuable insights, revealing the beneficial effects of open CdSe cores and CdS cosensitizers on the series resistance and recombination quality of CdS-HNR-cosensitized solar cells. The result is an optimized PCE of 5.89%, which is unmatched among anisotropic nanoparticle SSCs.

EXPERIMENTAL PROCEDURE

Synthesis of HNRs with Different Second-Component Coverages. Linear CdSe/$CdSe_xTe_{1-x}$ HNRs (*l*HNRs) and core/shell CdSe/$CdSe_xTe_{1-x}$ HNRs (*c*HNRs) were synthesized following our previous work.[13,14,19] In brief, a specified amount of CdO, *N*-octadecylphosphonic acid (ODPA), and trioctylphospine oxide was used to prepare the Cd−ODPA complex in a reaction vessel, after which the separately prepared Se−TOP and Te−TOP precursors were injected to grow the CdSe seed nanorods and the $CdSe_xTe_{1-x}$ second components on them. The injection solution for the second component contained Se and Te in a 4:1 ratio. Core/patchy-shell HNRs (*p*HNRs) were synthesized in the same manner as *c*HNRs, except that the amount of 0.33 M Se−TOP precursor used to form the CdSe seed was increased from 1.5 to 2 mL. For all HNRs, recapping with 1-octanethiol was carried out following our previous report.[7]

Preparation of Mesoporous TiO_2 (mp-TiO_2) Films. Spherical polystyrene (PS) microbead-incorporated TiO_2 nanoparticle paste was prepared according to our previous report with minor differences.[13,14] In brief, TiO_2 nanoparticles, PS microbeads, and ethyl cellulose were mixed with terpineol, and the final paste composition by weight ratio was TiO_2/PS/EC/terpineol = 1:0.5:1:8. Prepared TiO_2 paste was coated on cleaned fluorine-doped tin oxide (FTO) by doctor-blading and sintered at 450 °C for 30 min. Three layers of Scotch tapes were used to define the thickness of TiO_2 layer in coating the paste by the doctor-blade method.

CdS Growth by SILAR. CdS growth was carried out using the SILAR method.[14,20,21] For one cycle of CdS SILAR growth, electrodes were immersed into 0.05 M $Cd(CH_3COO)_2{\cdot}2H_2O$ solution and 0.05 M $Na_2S{\cdot}9H_2O$ solution. Each immersion took 1 min to complete. DIW/MeOH = 1:1 (v/v) mixture was used as the solvent to prepare the solutions and to rinse the electrodes after every single immersion.

Preparation of MPA−HNR−*n*CdS-Cosensitized mp-TiO_2 Electrodes. HNR loading on TiO_2 electrode was carried out by linker-assisted adsorption.[22−24] Annealed TiO_2 electrodes were treated in acetonitrile solution of 3-mercaptopropionic acid (MPA) as in our previous reports[13,14] After rinsing with acetonitrile, MPA-treated electrodes were immersed into HNR solution for 96 h.[13,14] After HNR loading, *n* SILAR cycles as indicated were applied for the postgrowth of CdS.

Preparation of 6CdS−HNR−*n*CdS-Cosensitized mp-TiO_2 Electrodes. CdS pregrowth on TiO_2 electrodes was carried out by applying six SILAR cycles described above. The number of pregrowth cycles of six was chosen from the optimum condition of our previous results.[14] HNR loading on CdS pregrown TiO_2 was carried out by two different methods. For the direct adsorption (DA) route,[25] the electrodes were immersed in HNR solution for 96 h. For the electrophoretic deposition (EP) route,[5,26] CdS pregrown TiO_2 electrode and FTO counter electrode were spaced ∼0.5 cm apart in the HNR solution and 200 V direct current (dc) bias was applied between electrodes using dc power supply (SDC2514R: PSPLASMA) for 20 min. The working electrode was connected to the negative terminal. After HNR loading, the electrodes were rinsed with toluene and another *n* SILAR cycles were applied for CdS postgrowth. Completed electrodes are designated as "6CdS−HNR(DA)−*n*CdS" or "6CdS−HNR(EP)−*n*CdS", according to the HNR loading method used.

ZnS Passivation and Solar Cell Assembly. Cosensitized electrodes were finally treated by ZnS growth by SILAR.[13,14] For the ZnS growth, the cosensitized electrodes were immersed in 0.1 M solution of $Zn(CH_3COO)_2{\cdot}2H_2O$ and 0.1 M solution of $Na_2S{\cdot}9H_2O$ for 1 min, respectively. DIW was used as the solvent to prepare the solutions, and five SILAR cycles were applied to grow ZnS. To fabricate Cu_xS counter electrodes,[13,14,25,27] brass foil pieces were polished with sandpaper, etched in HCl, and sulfurized with an aqueous polysulfide solution.[13,14] Completed cosensitized electrodes were assembled with counter electrode and polysulfide electrolyte to finish a sandwich-type cell. Electrolyte composition and spacer were the same as in our previous report.[13,14]

Characterization. The morphology and cross-sectional distribution of elements in sensitized electrodes were analyzed using a field-emission scanning electron microscope (Merlin-Compact: ZEISS). Transmission electron microscopy (TEM) to analyze different kinds of HNRs was carried out using a JEOL 2100 TEM with 200 kV operating voltage. Fast-Fourier transform (FFT) analysis was performed using a Gatan Digital Micrograph. The UV−vis absorption spectra of HNRs were measured with a photodiode array spectrometer (Agilent 8453; Agilent). The current density−voltage (J−V) curves were obtained using a potentiostat (Zive MP1: WonATech Co., Ltd, Korea), during which the solar cells were illuminated with AM 1.5 simulated sunlight (K3000: McScience, Korea, intensity at 100 mW cm^{-2}). Incident photon-to-current conversion efficiency (IPCE) spectra were measured with an IPCE measurement system (K3100: McScience, Korea). The UV−vis absorption spectra of sensitized electrodes were obtained with a UV−vis spectrometer (V-770: JASCO).

RESULTS AND DISCUSSION

Properties of CdSe/$CdSe_xTe_{1-x}$ Type-II HNRs with Different $CdSe_xTe_{1-x}$ Coverages. In order to study the effects of heterointerface area and core accessibility, we synthesized CdSe/$CdSe_xTe_{1-x}$ with varying shell coverage. CdSe nanorods were synthesized first in every case, and then a mixture of Se and Te precursors was injected slowly to grow the second component in a single pot. The absorption spectra of the heterostructures are shown in Figure 1a. Schematics, representative high-resolution TEM images, and FFT reconstructions highlighting the spatial distribution of components are shown in Figure 1b. Representative low-resolution TEM images are available in the Supporting Information, Figure S1. In the FFT reconstructions, smaller lattice components (CdSe) are colored green while larger lattice parameter components ($CdSe_xTe_{1-x}$) are colored magenta. The details of the FFT reconstructions are described

DOI: 10.1021/acsami.9b02873
ACS Appl. Mater. Interfaces XXXX, XXX, XXX−XXX

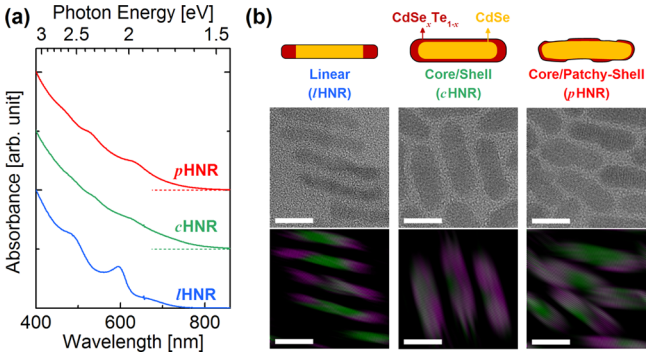

Figure 1. (a) Absorbance spectra of HNRs used in this study. From the bottom: linear HNR (lHNR) with $CdSe_xTe_{1-x}$ alloy tips, core/shell HNR (*c*HNR) with full-coverage alloy shell, and core/patchy-shell HNR (*p*HNR) with partial-coverage alloy shell. (b) Schematic illustration, typical high-resolution TEM image, and FFT reconstruction of lHNR, *c*HNR, and *p*HNR. In the FFT reconstructions, green indicates smaller lattice parameter, while magenta indicates larger lattice parameter. The scale bars are 10 nm.

in Figure S2. In the linear rod-rod-rod heterostructure (lHNR), which is grown at 250 °C, $CdSe_xTe_{1-x}$ extends out on both ends of the seed CdSe nanorod. The side facets of CdSe in *l*HNRs are fully exposed to the surface, but the heterointerface area is relatively small, and the absorption at wavelengths below the $CdSe_xTe_{1-x}$ band edge transition is correspondingly very weak. In the FFT reconstruction of the core/shell heterostructure (*c*HNR) in Figure 1b, which is grown at 300 °C, the CdSe core is not very distinct and large white regions representing intermediate lattice parameter are visible. The intermediate size lattice is expected with overlapping CdSe and $CdSe_xTe_{1-x}$ domains and supports complete (or nearly complete) shell structure of the *c*HNRs. There is also a prominent absorption tail extending out to the NIR region, indicative of the large interfacial area of *c*HNRs.

While *l*HNRs have both components physically accessible, they have relatively small heterointerface area that promotes charge separation. A significantly larger heterointerface area can be achieved with *c*HNRs but at the cost of having CdSe inaccessible for electron extraction. Core/patchy-shell HNRs (*p*HNRs) provide a relatively large heterointerface area while keeping a significant amount of CdSe accessible to the surface. The *p*HNRs are synthesized at 300 °C similar to *c*HNRs, but with 33% more Se precursor to form the initial seed CdSe nanorods, leaving less Cd available to grow $CdSe_xTe_{1-x}$. Rather than growing thinner uniform shell, this reaction condition leads to patchy shell growth. TEM observations show that *p*HNRs indeed exhibit irregular island growth on the sides unlike nearly uniform shell growth seen in *c*HNRs (Figure 1b). After examination of more than 100 individual rods from each batch, the average diameter through the center was found to be 6.71 ± 0.48 nm for *c*HNRs and 5.85 ± 0.61 nm for *p*HNRs. Not only is the shell thinner on average for *p*HNRs, the higher standard deviation implies a higher surface roughness, and the FFT reconstruction reveals that significantly more CdSe is accessible on the surface (Figure 1b).

Photovoltaic Performance of CdS-HNR-Cosensitized Solar Cells. HNRs with varying $CdSe_xTe_{1-x}$ shell coverage (*l*HNRs, *c*HNRs, and *p*HNRs) were first incorporated into the cosensitized device structure with only CdS postgrowth. The HNRs were adsorbed on TiO_2 with the assistance of MPA bifunctional linkers, and additional *n* cycles of SILAR were carried out for CdS postgrowth. Hereafter, we designate this kind of cosensitized electrode as "MPA−HNR−*n*CdS".

The *J*−*V* curves obtained from MPA−HNR−*n*CdS electrodes are presented in Figure 2a−c, and the photovoltaic parameters are listed in Table 1. *p*HNRs resulted in the most efficient devices, achieving a PCE of 4.50%. The IPCE spectra obtained from MPA−HNR−4CdS devices are compared in Figure 2d to investigate the effect of HNR structure on the spectral distribution of photocurrent generation. Compared to *l*HNRs, which have the smallest heterointerface area, the effect of full-coverage shell (*c*HNRs) is dramatic in the NIR region, where IPCE response is extended past 900 nm in wavelength. Such a spectral extension is attributed to the largest

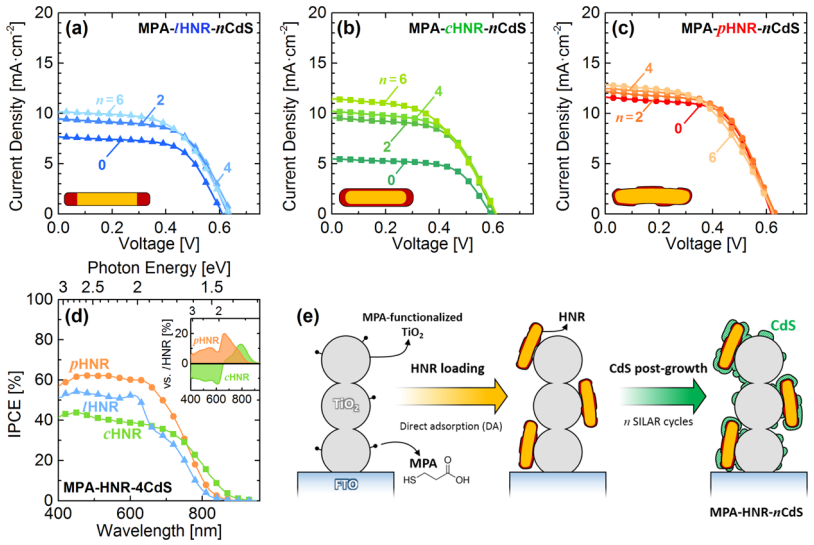

Figure 2. (a−c) *J*−*V* characteristics of MPA−HNR−*n*CdS cells, prepared by MPA-assisted adsorption of HNRs and successive postgrowth of CdS by the SILAR method. (d) IPCE spectra obtained from MPA−HNR−4CdS sensitized electrodes, where the amount of IPCE gain/loss resulted by tuning the morphology of HNRs from *l*HNRs to *c*HNRs or *p*HNRs is plotted in the inset, respectively. (e) Schematic illustration of the procedure for preparing MPA−HNR−*n*CdS electrodes.

DOI: 10.1021/acsami.9b02873
ACS Appl. Mater. Interfaces XXXX, XXX, XXX−XXX

Table 1. Photovoltaic Parameters of MPA−HNR−*n*CdS-Cosensitized Solar Cells Fabricated Using Differently Structured HNRs

structure	J_{sc} [mA·cm^{-2}]	V_{oc} [V]	FF	PCE [%]
MPA−lHNR−0CdS	7.64 ± 0.30	0.61 ± 0.00	0.62 ± 0.01	2.90 ± 0.14
MPA−lHNR−2CdS	9.47 ± 0.26	0.63 ± 0.00	0.61 ± 0.01	3.62 ± 0.11
MPA−lHNR−4CdS	9.42 ± 0.43	0.64 ± 0.00	0.60 ± 0.00	3.62 ± 0.19
MPA−lHNR−6CdS	10.18 ± 0.27	0.63 ± 0.00	0.56 ± 0.00	3.64 ± 0.10
MPA−*c*HNR−0CdS	5.48 ± 0.43	0.59 ± 0.00	0.62 ± 0.01	2.02 ± 0.16
MPA−*c*HNR−2CdS	9.57 ± 0.21	0.61 ± 0.00	0.58 ± 0.01	3.38 ± 0.04
MPA−*c*HNR−4CdS	10.23 ± 0.40	0.61 ± 0.00	0.56 ± 0.01	3.52 ± 0.08
MPA−*c*HNR−6CdS	11.47 ± 0.09	0.61 ± 0.00	0.51 ± 0.00	3.59 ± 0.01
MPA−*p*HNR−0CdS	11.68 ± 0.50	0.62 ± 0.00	0.60 ± 0.01	4.37 ± 0.23
MPA−*p*HNR−2CdS	12.36 ± 0.52	0.63 ± 0.00	0.58 ± 0.02	4.50 ± 0.11
MPA−*p*HNR−4CdS	12.54 ± 0.54	0.63 ± 0.01	0.55 ± 0.01	4.31 ± 0.21
MPA−*p*HNR−6CdS	12.91 ± 0.30	0.63 ± 0.00	0.51 ± 0.01	4.10 ± 0.18

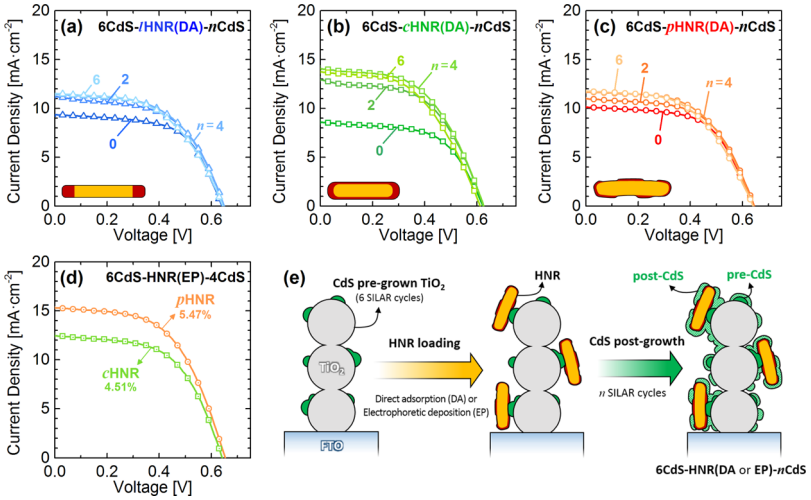

Figure 3. (a−c) *J*−*V* characteristics of 6CdS−HNR(DA)−*n*CdS cells and (d) 6CdS−HNR(EP)−4CdS cells, prepared by loading HNRs on CdS pregrown TiO_2 electrode by DA or EP and successive postgrowth of CdS by the SILAR method. (e) Schematic illustration of the procedure for preparing 6CdS−HNR(DA)−*n*CdS and 6CdS−HNR(EP)−*n*CdS electrodes.

Table 2. Photovoltaic Parameters of 6CdS−HNR(DA)−*n*CdS-Cosensitized Solar Cells Fabricated Using Differently Structured HNRs

structure	J_{sc} [mA·cm^{-2}]	V_{oc} [V]	FF	PCE [%]
6CdS	4.57 ± 0.03	0.63 ± 0.01	0.59 ± 0.01	1.69 ± 0.01
6CdS−lHNR(DA)−0CdS	10.05 ± 0.77	0.64 ± 0.01	0.59 ± 0.02	3.79 ± 0.23
6CdS−lHNR(DA)−2CdS	11.23 ± 0.40	0.65 ± 0.00	0.55 ± 0.01	4.00 ± 0.12
6CdS−lHNR(DA)−4CdS	11.46 ± 0.37	0.65 ± 0.01	0.55 ± 0.00	4.06 ± 0.11
6CdS−lHNR(DA)−6CdS	11.87 ± 0.03	0.64 ± 0.00	0.52 ± 0.01	4.00 ± 0.01
6CdS−*c*HNR(DA)−0CdS	8.83 ± 0.53	0.63 ± 0.01	0.59 ± 0.00	3.13 ± 0.05
6CdS−*c*HNR(DA)−2CdS	12.95 ± 0.53	0.62 ± 0.00	0.54 ± 0.01	4.33 ± 0.22
6CdS−*c*HNR(DA)−4CdS	14.07 ± 0.37	0.63 ± 0.01	0.52 ± 0.00	4.61 ± 0.07
6CdS−*c*HNR(DA)−6CdS	13.76 ± 0.36	0.61 ± 0.00	0.50 ± 0.01	4.25 ± 0.05
6CdS−*p*HNR(DA)−0CdS	10.11 ± 0.35	0.64 ± 0.00	0.59 ± 0.01	3.85 ± 0.15
6CdS−*p*HNR(DA)−2CdS	11.00 ± 0.37	0.65 ± 0.00	0.57 ± 0.00	4.07 ± 0.13
6CdS−*p*HNR(DA)−4CdS	11.70 ± 0.43	0.64 ± 0.00	0.55 ± 0.00	4.16 ± 0.14
6CdS−*p*HNR(DA)−6CdS	11.74 ± 0.14	0.64 ± 0.00	0.53 ± 0.02	3.96 ± 0.23

heterointerface of *c*HNRs contributing to NIR photon harvesting by charge-separated state (CSS) absorption.[6,7,12−14] However, the photocurrent contribution from the visible wavelength region shorter than ∼650 nm is reduced, which can be attributed to the detrimental effect of a full-coverage shell inhibiting facile electron extraction from the CdSe core.[14] On the other hand, by using *p*HNRs, which are engineered to have an exposed CdSe core, photocurrent from the vis-to-NIR region is all improved compared with lHNR counterparts (inset of Figure 2d).

Inspection of V_{oc} (Figure 2a−c and Table 1) shows that V_{oc} values are lowest with *c*HNRs and highest with *l*HNRs. The smallest V_{oc} deficit of lHNR devices implies that the facile electron extraction from the exposed CdSe core effectively

DOI: 10.1021/acsami.9b02873
ACS Appl. Mater. Interfaces XXXX, XXX, XXX−XXX

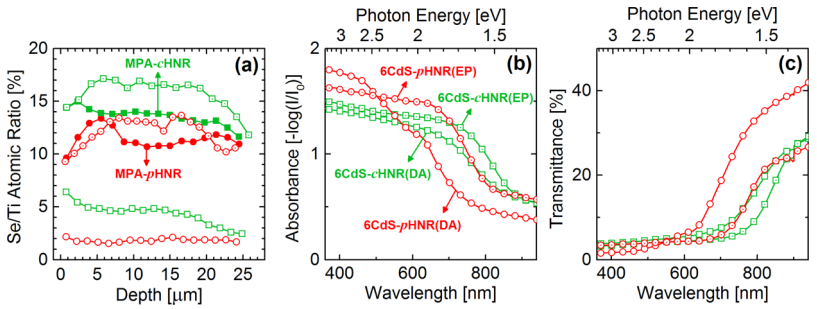

Figure 4. Comparison of *c*HNR- and *p*HNR-sensitized TiO_2 electrodes. (a) Depth profile of Se/Ti atomic ratio obtained by cross-sectional SEM−EDS measurements. (b,c) Absorption and transmittance spectra of *p*HNR- and *c*HNR-sensitized electrodes prepared by DA or EP methods.

Table 3. Photovoltaic Parameters of 6CdS−HNR(EP)−4CdS-Cosensitized Solar Cells Fabricated Using Differently Structured HNRs

structure	J_{sc} [mA·cm^{-2}]	V_{oc} [V]	FF	PCE [%]
6CdS−*c*HNR(EP)−4CdS	12.45 ± 0.19	0.64 ± 0.00	0.56 ± 0.01	4.51 ± 0.13
6CdS−*p*HNR(EP)−4CdS	15.31 ± 0.18	0.65 ± 0.00	0.55 ± 0.01	5.47 ± 0.10

suppresses the recombination. V_{oc} from *p*HNR devices quite resembles that from *l*HNRs, further supporting that the open-core structure is preferred to suppress the recombination in HNRs.

Having confirmed that *p*HNRs outperform other kinds of HNR structures with linker-assisted HNR adsorption and CdS postgrowth, we next examined the CdS−HNR-cosensitized electrode configuration where the SILAR growth of CdS is applied both before and after HNR loading. HNRs were loaded on TiO_2 electrodes with pregrown CdS processed by six SILAR cycles, and *n* SILAR cycles of postgrown CdS were carried out. HNRs were first loaded on CdS pregrown TiO_2 by DA,[25] and hereafter, we refer to this kind of cosensitized electrode as "6CdS−HNR(DA)−*n*CdS". In this configuration, the HNR loading was not assisted by MPA linkers, as the MPA treatment on CdS-grown TiO_2 led to the decomposition of CdS.[14] The *J*−*V* curves from 6CdS−HNR(DA)−*n*CdS devices are presented in Figure 3a−c, and the photovoltaic parameters are listed in Table 2. For the 6CdS−HNR(DA)−*n*CdS configuration, the best performance resulted from *c*HNRs rather than from *p*HNRs in contrast to the MPA−HNR−*n*CdS cases. This is due to the limitation of HNR loading by the DA route, which is far lower than MPA-assisted loading where the chemisorption sites are provided by bifunctional MPA linkers. The loading amounts of *c*HNRs and *p*HNRs by different deposition strategies were compared by measuring the cross-sectional SEM−EDS and absorbance/transmittance measurements, which are presented in Figure 4. The results show that the loading amount of *p*HNRs by the DA route is the lowest, resulting in the smallest Se/Ti ratio throughout the electrode and correspondingly low absorption of sensitized film. To improve this limitation, EP was applied to increase the HNR loading amount with the assistance of an electric field.[5,26] As the four cycles of SILAR for the postgrown CdS led to the best device performance for all kinds of HNRs in the 6CdS−HNR(DA)−*n*CdS electrode structure, four cycles of CdS SILAR were applied for the electrodes with EP-loaded HNRs. These samples are hereafter referred to as "6CdS−HNR(EP)−4CdS" devices. The *J*−*V* characteristics and photovoltaic parameters (Figure 3d and Table 3) show that *p*HNRs exceed *c*HNRs in performance and reach a PCE of 5.47%, which is improved by ∼20% compared with the best *p*HNR cell (4.50%) from the MPA-assisted method. Such a high efficiency is unmatched among the SSCs based on anisotropic colloidal semiconductor nanocrystal light harvesters.

Role of HNR Structure and CdS Cosensitization: Insights from One-Diode Model Analysis. To further investigate the effect of HNR structures and CdS cosensitizers on the photovoltaic performance of CdS−HNR-cosensitized devices, one-diode model analysis was carried out.[28−30] The well-known one-diode model equation

$$J = J_{ph} - J_0\left[\exp\left(\frac{q\beta(V + JR_s)}{k_BT}\right) - 1\right] - \frac{V + JR_s}{R_{sh}} \quad (1)$$

was used to fit the measured *J*−*V* curves, where J_{ph} is the photogenerated current density, J_0 is the diode saturation current density, β is the recombination order (reciprocal of the ideality factor), R_s is the series resistance, R_{sh} is the shunt resistance, and k_BT/q is the thermal voltage. Here, we note that we used the explicit form of eq 1 containing Lambert−W function for actual fitting.[29] The photovoltaic parameters and one-diode model parameters obtained by *J*−*V* curve fitting are presented in Figure 5. First of all, a notable trend is observed from the series resistance (R_s). MPA−*p*HNR−0CdS and MPA−lHNR−0CdS devices show smaller R_s than MPA−*c*HNR−0CdS devices, which reflects the feature that HNRs with open CdSe cores are more likely to form TiO_2−CdSe contact, which is more favorable for electron extraction. Continued postgrowth of CdS leads to the J_{sc} increase for all types of HNRs.

Compared to MPA−HNR−*n*CdS devices, which exhibit R_s of ∼10 Ω·cm^2 or higher, 6CdS−HNR−*n*CdS devices show significantly reduced R_s. This effect of R_s reduction is most drastic for lHNR devices, where the R_s value is lowered down to ∼6 Ω·cm^2. *c*HNR devices show the highest R_s values, further confirming that their full-coverage shell inhibiting facile electron extraction deteriorates the device performance. This feature should be responsible for the low fill factor (FF) of the resulting devices. Inspection of the shunt resistance (R_{sh}) shows that improved R_{sh} results from appropriate cosensitization, which should lead to the improved FF.

Investigation of the diode quality parameters, the diode saturation current density (J_0) and recombination order (β),

DOI: 10.1021/acsami.9b02873
ACS Appl. Mater. Interfaces XXXX, XXX, XXX−XXX

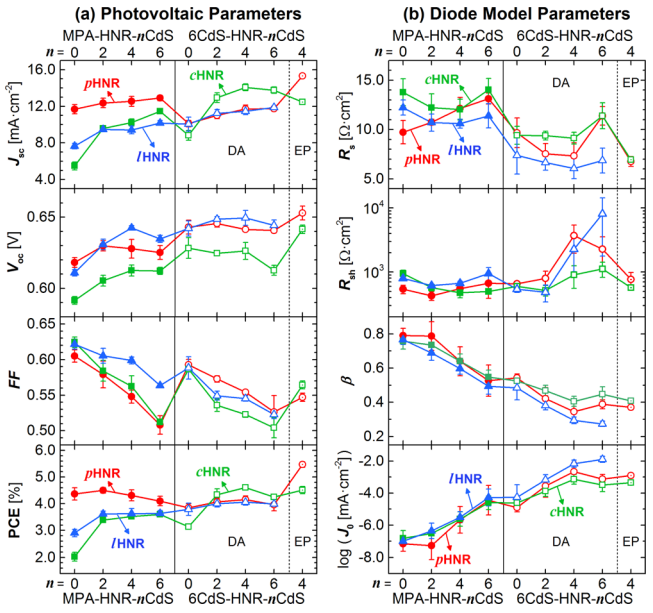

Figure 5. (a) Photovoltaic parameters [short-circuit current density (J_{sc}), open-circuit voltage (V_{oc}), FF, and PCE] and (b) ideal one-diode model parameters {series resistance (R_s), shunt resistance (R_{sh}), recombination order [β = (ideality factor)$^{-1}$], and diode saturation current density (J_0)} obtained from HNR-SSCs.

provides another valuable perspective. Most of all, cosensitization with CdS leads to almost monotonic decrease (deterioration) of β as more CdS SILAR cycles are applied, which means that the recombination process is moved far from ideal recombination of free electrons. The J_0 values increase accordingly, implying that the CdS incorporated by SILAR aggravates the recombination. A similar trend of reduction in β and increase in J_0 was observed in our previous report.[14] This is likely due to the holes remaining in CdS after photoexcitation, which can be caused by fast hole trapping kinetics of CdS grown by SILAR.[31] Even though it has been reported that the elaborated CdS layer over QDs by epitaxial growth can significantly reduce surface defects,[32] in our case, the growth of many CdS layers led to more recombination due to the defective feature of solution-processed CdS. This deterioration is accompanied by a reduction of R_s, establishing a trade-off between transport and recombination properties of CdS−HNR-cosensitized electrodes.

Further investigation of the recombination quality parameters β and J_0 leads to a complication when we try to correlate these parameters to the photovoltaic performance. Especially for 6CdS−HNR(DA)−nCdS and 6CdS−HNR(EP)−4CdS devices, it is seen that the β values are in the order of lHNR < pHNR < cHNR and J_0 values are in the reverse order. At a glance, such a trend seems to provide a straightforward interpretation that cHNRs suffer the least from recombination and lHNRs suffer the most in these cosensitized electrodes, which may lead to the conclusion that providing $CdSe_xTe_{1-x}$ shells with higher coverage systematically suppresses the recombination in the cosensitized electrode. Justifications of this kind, which attribute the better device-performance parameters to the improved diode-quality parameters, can be frequently found in literature studies.[33−36] However, considering Figure 5a, one cannot make such justification based on the diode-model analysis results. Even though the cHNRs exhibit the highest efficiency in 6CdS−HNR(DA)−nCdS configuration, it is not the case for 6CdS−HNR(EP)−4CdS configuration. Furthermore, the V_{oc} values from cHNR devices never exceed those from less-shelled HNRs (Figure 5a), which also cannot be justified based on the simple rule of thumb that more-ideal (β close to 1) and less-severe (lower J_0) recombination parameters guarantee better photovoltaic performance including V_{oc}. These observations imply that recombination processes in CdS−HNR-cosensitized electrodes are more subtle and should be better understood in order to provide a more consistent explanation based on the diode model analysis.

Given this perspective, we have noticed that the variations of β and J_0 in Figure 5b are highly correlated. When β varies, log J_0 does by quite a similar scale. This observation led us to construct a plot showing the intercorrelation structure between

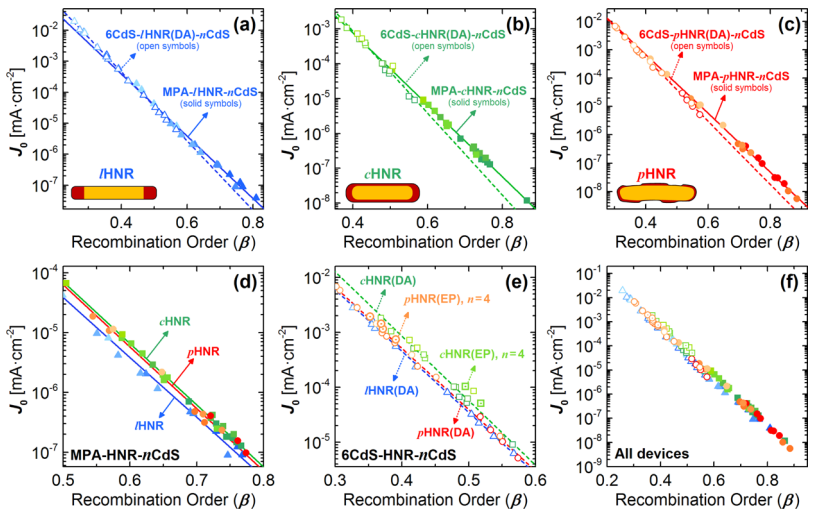

Figure 6. (a−c) J_0 vs β intercorrelation plots of (a) lHNR devices, (b) cHNR devices, and (c) pHNR devices. Solid and dashed lines in each panel show linear fit through MPA−HNR−nCdS or 6CdS−HNR(DA)−nCdS-cosensitized devices, respectively. (d,e) Merged J_0 vs β plots showing (d) MPA−HNR−nCdS devices and (e) 6CdS−HNR−nCdS devices, where the lines are same with those in preceded panels. Note that in panel (e), 6CdS−HNR(EP)−4CdS devices are just overlaid for comparison with 6CdS−HNR(DA)−nCdS devices and not used to provide fitting lines. (f) Merged J_0 vs β plot showing all the devices studied in this work.

DOI: 10.1021/acsami.9b02873
ACS Appl. Mater. Interfaces XXXX, XXX, XXX−XXX

Table 4. $k_{rec,0}$ and Λ Values Obtained from Linear Fitting Lines Drawn in J_0 vs β Intercorrelation Plots (Figure 6a−c) with Eq 4[a]

	MPA−HNR−*n*CdS		6CdS−HNR(DA)−*n*CdS	
	$k_{rec,0}$ [10^{21} $cm^{-3(1-\beta)}.s^{-1}$]	Λ [eV]	$k_{rec,0}$ [10^{21} $cm^{-3(1-\beta)}.s^{-1}$]	Λ [eV]
lHNR	8.3 ± 2.9	0.60 ± 0.01	27.4 ± 2.2	0.66 ± 0.01
*c*HNR	21.3 ± 4.3	0.61 ± 0.01	87.8 ± 41.6	0.70 ± 0.03
*p*HNR	19.7 ± 3.8	0.62 ± 0.01	30.1 ± 03.5	0.66 ± 0.01

[a] L = 30 μm was used to estimate $k_{rec,0}$.

these two variables. In Figure 6, each point on the plot shows a (β, J_0) pair obtained from one-diode model fit of single J−V curve. Hereafter, we will call this kind of semi-log plot as J_0 versus β intercorrelation plot or simply the J_0 versus β plot. It is seen that quite strong linear correlation exists on these semi-log plots, and the slope and intercepts of which appear dependent on the electrode configuration. For example, Figure 6a−c shows that lines of different slopes and intercepts describe the MPA−HNR−*n*CdS devices (filled symbols with solid line) and 6CdS−HNR−*n*CdS devices (open symbols with dashed line). The latter has a steeper slope. Figure 6d,e presents these lines in a different manner, showing devices with the same configurations (MPA−HNR−*n*CdS or 6CdS−HNR−*n*CdS) in a single plot. From these plots we see that the J_0 values at a given β value are in the order of lHNR < *p*HNR < *c*HNR. From eq 1, it is obvious that at a fixed β the lower J_0 should result in higher V_{oc}. Therefore, this trend is a straightforward illustration of the reason why *c*HNR devices never outperform other HNRs with less-coverage shells especially in terms of V_{oc}.

We now proceed to extract more quantitative information from these plots. Although the strong linear correlation observed cannot be understood solely from eq 1, the formulation of J_0 from the work of Bisquert et al. provides a useful guide to understanding such behavior.[37] In their work, J_0 is given by following expression:

$$J_0 = qk_{rec}LN_c^{\beta}\exp\left(\frac{E_{F0}\beta}{k_BT}\right)\exp\left(\frac{-E_c\beta}{k_BT}\right) \quad (2)$$

where L is the thickness of absorber layer (sensitized TiO_2 film in our case), N_c (=$2(m_ek_BT/2\pi\hbar^2)^{3/2}$) is the effective density of states for electrons in TiO_2 conduction band, E_c is the conduction band edge of TiO_2, and E_{F0} is the Fermi level at dark equilibrium state, which is assumed to be equilibrated with the redox potential of the electrolyte species. This expression is derived by assuming that the recombination rate U_n is dependent on the free carrier concentration (n) powered by a unitless constant β ($U_n = k_{rec}n^{\beta}$), which is introduced to explain any deviation from linear recombination behavior ($U_n = k_{rec}n$).[37−39] In using eq 2, Bisquert et al. treated the prefactor of $\exp(-E_c\beta/k_BT)$ as an independent parameter. Such an approach allowed them to simplify the complex features entangled in eq 2 and focus on the effect of other important parameters, such as E_c and β.

To analyze our J_0 versus β plots, we rearranged eq 2 into the form where all the parameters containing β are collected in the argument of a single exponential function. This rearrangement can be done by defining nondimensionalized N_c as $\tilde{N}_c = N_c/N_o$ and choosing N_o to be 1 cm^{-3}. The rearranged form of J_0 is given by

$$J_0 = qk_{rec}LN_o^{\beta}\exp\left(-\frac{(E_c - E_{F0} - k_BT\ln\tilde{N}_c)\beta}{k_BT}\right) \quad (3)$$

As above choice of N_o makes the N_o^{β} term in prefactor yield unity irrespective of β, eq 3 can be used to explain the observed linear correlations. The β = 0 intercept and slope of linear fitting lines drawn on Figure 6a−c can be interpreted based on this equation.

As will be explained with Table 4, the slopes obtained from these fitting lines require $E_c - E_{F0} - k_BT\ln\tilde{N}_c$ to be 0.6−0.7 eV if we use eq 3. However, the literature generally gives the values of $E_c - E_{F0} < 1$ eV and $N_c > 10^{19}$ cm^{-3}, which forces the $E_c - E_{F0} - k_BT\ln\tilde{N}_c$ value to be smaller than −0.13 eV at T = 300 K.[37,40−43] This implies that k_{rec} in our CdS−HNR-cosensitized system cannot be constant but should have exponential dependence on β, for example, $k_{rec} = k_{rec,0}\exp(-\delta\beta/k_BT)$, to achieve the observed slope. Correction of eq 3 with the empirical parameter δ leads to the final expression

$$J_0 = qk_{rec,0}LN_o^{\beta}\exp\left(-\frac{(E_c - E_{F0} - k_BT\ln\tilde{N}_c + \delta)\beta}{k_BT}\right) = qk_{rec,0}LN_o^{\beta}\exp\left(-\frac{\Lambda\beta}{k_BT}\right) \quad (4)$$

where $\Lambda = E_c - E_{F0} - k_BT\ln\tilde{N}_c + \delta$, which we used to interpret the linear behaviors in Figure 6.

$k_{rec,0}$ and Λ obtained from linear fit lines in Figure 6 are listed in Table 4, where L = 30 μm was used to calculate $k_{rec,0}$. When the lines with similar Λ are compared, $k_{rec,0}$ can be understood as the recombination rate constant inherent to a system as the lower J_0 should result at the given β if the system has lower $k_{rec,0}$. Such a comparison holds for our HNR-sensitized devices for a given configuration, as shown in Figure 6d,e. *c*HNRs exhibit the largest $k_{rec,0}$, meaning that *c*HNR-based devices are most vulnerable to the recombination. *l*HNRs show the smallest $k_{rec,0}$, meaning that HNRs with open CdSe cores suffer the least from recombination. Increases of Λ by 0.04−0.09 eV, which are accompanied by the change in electrode configuration from MPA−HNR−*n*CdS to 6CdS−HNR(DA)−*n*CdS, can arise from changes in all or some of the four parameters merged into Λ. Among these parameters, E_{F0} and $\tilde{N}_c$ are less likely to be affected by CdS growth, as these values are characteristic to the electrolyte and TiO_2. Furthermore, it is known that the CdS growth by SILAR can lower its E_c of TiO_2 by reducing the TiO_2−electrolyte contact area.[39] Therefore, the observed increase of Λ should be mostly due to an increase in δ. That is, k_{rec} increases more steeply by postgrown CdS in the 6CdS−HNR(DA)−*n*CdS system, meaning that the pregrown CdS accelerates recombination in cosensitized solar cells.

DOI: 10.1021/acsami.9b02873
ACS Appl. Mater. Interfaces XXXX, XXX, XXX−XXX

While details such as the physical origin of δ need further investigation, this approach based on the J_0 versus β plot provides a different interpretation for the recombination processes in CdS−HNR-cosensitized electrodes. On the basis of J_0 versus β plots, we can say that the reason why *p*HNRs are optimal is not because the increased shell coverage is beneficial for suppressing the recombination. Proper interpretation is rather the opposite: *c*HNRs are the most vulnerable to recombination among HNR structures studied, and open CdSe cores rather than shielded CdSe cores are more desirable for suppressing recombination. From the type-II nature of HNRs, *c*HNRs should suffer inherently more severe recombination as the electrons confined in the CdSe core are difficult to extract and more likely to recombine with holes. *p*HNRs suffer less from such a problem because the open CdSe core enables facile electron extraction by the formation of cascade structure such as TiO_2−CdS−CdSe−$CdSe_xTe_{1-x}$ and leads to suppressed recombination (lower $k_{rec,0}$). Such an interpretation is not possible when J_0 and β are examined individually (Figure 5b).

There is a final question that remains unanswered: then why do the *c*HNR devices present more desirable diode quality parameters, namely β closer to unity and lower J_0, at the same number of CdS SILAR cycles applied? Because of the marginal amount of traps in our colloidal HNRs, the recombination process occurring inside the HNRs should have characteristic β quite close to unity. This can be indirectly seen from Figure 5b, where the CdS-free devices (MPA−HNR−0CdS) show the β values quite close to 1. When cosensitized with CdS, HNRs with exposed CdSe cores readily form TiO_2−CdS−CdSe cascade alignment. As this alignment makes it easier to extract electrons from the CdSe cores of HNRs, photo-excited electrons are less likely to recombine inside HNRs but more likely to undergo CdS-related recombination having lower characteristic β. *c*HNRs cannot form such a contact due to the full-coverage shell, and the result is that electrons confined in CdSe cores are less likely to undergo CdS-related recombination. This causes the observed β to be closer to unity at the same CdS SILAR cycles applied. The important point is that this high β and apparently low J_0 do not always guarantee optimally suppressed recombination. This feature, as we have shown in this section, can be quantified by constructing J_0 versus β plots and introducing $k_{rec,0}$ and Λ. The role of HNR structures with varying exposure of the CdSe core is schematically summarized in Figure 7. As the CdS grown prior to HNR loading did not lessen the J_{sc} of cosensitized devices and even leads to the lower device R_s in diode model analysis, we infer that the conduction band edge of CdS is located lower than that of CdSe. Such a cascade band alignment has been experimentally confirmed to be possible and also has been known to be realized due to the Fermi level alignment.[17,26,44,45]

Even though the core/patchy-shell structure we present in this work is an improvement from the core/shell structure where the band alignment causes electrons to be localized in the core after photo-excitation, it is questionable whether this approach would lead to similar improvement for the case where the carriers localized in the core are holes rather than electrons. It has been well known that type-II QDs can benefit from the holes localized in the core. The delayed harvesting of localized holes by electrolyte is known to reduce the recombination between TiO_2 and electrolyte, and the localized holes are also known to induce dipole moment which upshifts

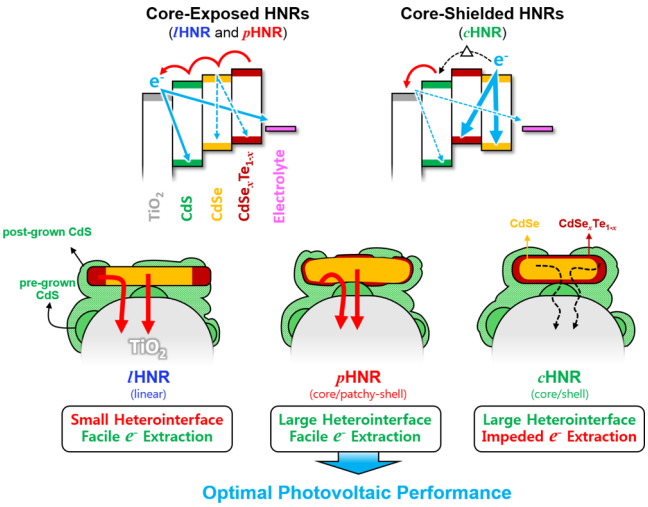

Figure 7. Schematic illustration showing the effect of *patchy-shell* morphology in CdS−HNR-cosensitized solar cell structure. Core/shell HNRs have sufficient heterointerface which contributes to NIR light harvesting. However, the full-coverage shell inhibits the extraction of photo-excited electrons in CdSe cores and such confined electrons undergo recombination which reduce the V_{oc} output of solar cells. Linear HNRs less suffer such problem due to its open structure and easier electron extraction from CdSe core, but the J_{sc} from HNRs of this kind is limited by the small type-II heterointerface area which is insufficient to harvest low-energy photons from sunlight. Core/patchy-shell structure, containing sufficiently large heterointerface area without the core CdSe component being completely shielded, enables the optimal performance by meeting both requisites of optimal light harvesting and facile carrier extraction.

the conduction band of TiO_2 causing a V_{oc} increase.[46−50] Wang et al. reported 6.76% efficient CdTe/CdSe core/shell QD SSCs with 0.606 V V_{oc}, and Jiao et al. reported the record device having 7.17% PCE and 0.642 V V_{oc} by tuning the composition of core/shell QDs from CdTe/CdSe to ZnTe/CdSe.[46,47] Even though the PCE of our best device still lags behind that of these record type-II QDs, it is promising that the V_{oc} of *p*HNR-only devices (0.62 V) exceeds that of CdTe/CdSe QD-based devices and even comparable to that of record devices from ZnTe/CdSe QDs with support of CdS cosensitization (0.65 V) considering the device structures presented in these works are similar to ours. Considering the high PCE based on these core/shell QDs, however, the role of patchy-shell structure and cosensitization we suggest here still needs further investigation in comparison with the hole-localizing type-II system to figure out whether the benefit of facilitated carrier extraction genuinely have potential to outcompete that of core-localized holes.

Although *p*HNR-based devices are promising in terms of V_{oc}, their J_{sc} (15.31 mA·cm^{-2}) is lower than that of the record core/shell QD devices referred above (~20 mA·cm^{-2}).[48,49] To provide further confidence to the potential of HNR-based photovoltaics, we further examined the effect of pore structure of TiO_2 electrodes on the photovoltaic performance. We inferred that our use of PS microbeads to provide interconnected large pores in TiO_2 electrode, which was effective to infiltrate HNRs throughout TiO_2 electrode in our previous reports,[13,14] could have ended up limiting the HNR loading amount when we aided HNR infiltration by EP. We prepared four kinds of TiO_2 electrodes having different combinations of layers derived from TiO_2 pastes with-or-

DOI: 10.1021/acsami.9b02873
ACS Appl. Mater. Interfaces XXXX, XXX, XXX−XXX

without PS additives (Figure S3a) and examined 6CdS−*p*HNR(EP)−4CdS-cosensitized devices made out of those electrodes. Even this simple modification improved the PCE of 6CdS−HNR(EP)−4CdS devices up to 5.89% (Figure S3b and Table S1), mainly due to the increase of J_{sc} up to ∼17 mA·cm^{-2} (Figure S3c). It should be noted that such improvement was achieved by applying lower bias voltage (∼10 V) for longer duration (96 h) during EP compared to the condition applied for the devices presented in Figure 3d. This suggests that the EP condition need to be optimized appropriately according to the pore structure of electrodes. We believe that further investigation of loading strategies and appropriate electrode pore structure for one-dimensionally elongated anisotropic sensitizers would lead to further improvement, achieving the PCE comparable to core/shell QD sensitizers. The lack of optimized TiO_2 electrode structure and appropriate sensitizer loading methods/conditions could also be the reason why non-QD semiconductor nanocrystal sensitizers have exhibited PCE lower than QD sensitizers.[5,51,52] Furthermore, there have also been breakthroughs regarding all the constituents of SSCs such as QD/electrode coating, electrolyte, and counter electrodes, which led to record PCEs in QD-based solar cells exceeding 12% and V_{oc} approaching 0.8 V.[53−57] All these strategies should be thoroughly considered and appropriately applied to improve the HNR-based PVs toward the next stage.

CONCLUSIONS

$CdSe/CdSe_xTe_{1-x}$ type-II HNRs were successfully engineered to have core/patchy-shell morphology. A sufficiently large heterointerface area led to increased light harvesting from the NIR region, without sacrificing that from the vis-region by having open CdSe cores. An efficiency of 5.47% (5.89% with modified electrode configuration) in the SSCs was achieved using optimally structured light harvesters with CdS cosensitizers, which is unmatched among the SSCs utilizing anisotropic colloidal nanoparticles as light harvesting materials. One-diode model analysis reveals major benefits of open-core HNR structures and CdS cosensitization: (1) the reduction of R_s especially emphasized with pre-grown CdS and (2) facilitated charge extraction which suppresses recombination within HNRs. Importantly, the latter interpretation was justified by investigating the diode quality parameters J_0 and β in terms of their intercorrelation than simply considering them individually. Furthermore, considering that CdS−HNR-cosensitized electrodes fabricated in this work exhibited relatively lower β, presumably due to the defective structure of CdS, strategies to modify the CdS cosensitizers in a similar system might enable better performing devices.

ASSOCIATED CONTENT

Supporting Information

The Supporting Information is available free of charge on the ACS Publications website at DOI: 10.1021/acsami.9b02873.

Representative TEM images of HNRs; description of FFT−IFFT procedure to separate regions of different lattice parameters from TEM images; and performance and photovoltaic parameters of 6CdS−*p*HNR(EP)−4CdS-cosensitized solar cells fabricated using different electrode configurations (PDF)

AUTHOR INFORMATION

Corresponding Authors

*E-mail: mshim@illinois.edu. Phone: +1-217-333-7361 (M.S.).

*E-mail: byungwoo@snu.ac.kr. Phone: +82-2-880-8319 (B.P.).

ORCID

Sangheon Lee: 0000-0001-8620-8213

Jaewook Kim: 0000-0002-7692-3990

Alan Jiwan Yun: 0000-0002-8661-5545

Byungho Lee: 0000-0002-4399-571X

Moonsub Shim: 0000-0001-7781-1029

Byungwoo Park: 0000-0002-3776-4392

Author Contributions

S.L. and J.C.F. contributed equally to this work. S.L. fabricated and analyzed the solar cells and participated in writing the paper. J.C.F. synthesized and characterized the HNRs and participated in writing the paper. J.K. contributed to tuning the HNR loading conditions and participated in writing the paper. A.J.Y. and B.L. participated in device characterization and writing the paper. M.S. and B.P. guided the project with crucial comments and participated in writing the paper.

Notes

The authors declare no competing financial interest.

ACKNOWLEDGMENTS

This work is supported by the National Research Foundation of Korea (NRF: 2016R1A2B4012938), Korea Institute of Energy Technology Evaluation and Planning (KETEP: 20183010014470), and the U.S. NSF (grant no. 1808163). SEM was carried out in the Research Institute of Advanced Materials (RIAM) at Seoul National University, and TEM was carried out in the Frederick Seitz Materials Research Laboratory Central Facilities at the University of Illinois.

REFERENCES

(1) Achtstein, A. W.; Antanovich, A.; Prudnikau, A.; Scott, R.; Woggon, U.; Artemyev, M. Linear Absorption in CdSe Nanoplates: Thickness and Lateral Size Dependency of the Intrinsic Absorption. *J. Phys. Chem. C* **2015**, *119*, 20156−20161.

(2) Davis, N. J. L. K.; Böhm, M. L.; Tabachnyk, M.; Wisnivesky-Rocca-Rivarola, F.; Jellicoe, T. C.; Ducati, C.; Ehrler, B.; Greenham, N. C. Multiple-Exciton Generation in Lead Selenide Nanorod Solar Cells with External Quantum Efficiencies Exceeding 120%. *Nat. Commun.* **2015**, *6*, 8259.

(3) Padilha, L. A.; Stewart, J. T.; Sandberg, R. L.; Bae, W. K.; Koh, W.-K.; Pietryga, J. M.; Klimov, V. I. Aspect Ratio Dependence of Auger Recombination and Carrier Multiplication in PbSe Nanorods. *Nano Lett.* **2013**, *13*, 1092−1099.

(4) Shabaev, A.; Efros, A. L. 1D Exciton Spectroscopy of Semiconductor Nanorods. *Nano Lett.* **2004**, *4*, 1821−1825.

(5) Salant, A.; Shalom, M.; Tachan, Z.; Buhbut, S.; Zaban, A.; Banin, U. Quantum Rod-Sensitized Solar Cell: Nanocrystal Shape Effect on the Photovoltaic Properties. *Nano Lett.* **2012**, *12*, 2095−2100.

(6) McDaniel, H.; Pelton, M.; Oh, N.; Shim, M. Effects of Lattice Strain and Band Offset on Electron Transfer Rates in Type-II Nanorod Heterostructures. *J. Phys. Chem. Lett.* **2012**, *3*, 1094−1098.

(7) Flanagan, J. C.; Shim, M. Enhanced Air Stability, Charge Separation, and Photocurrent in CdSe/CdTe Heterojunction Nanorods by Thiols. *J. Phys. Chem. C* **2015**, *119*, 20162−20168.

(8) Jiang, Y.; Cho, S.-Y.; Shim, M. Light-Emitting Diodes of Colloidal Quantum Dots and Nanorod Heterostructures for Future Emissive Displays. *J. Mater. Chem. C* **2018**, *6*, 2618−2634.

DOI: 10.1021/acsami.9b02873
ACS Appl. Mater. Interfaces XXXX, XXX, XXX−XXX

(9) Cho, S.-Y.; Oh, N.; Nam, S.; Jiang, Y.; Shim, M. Enhanced Device Lifetime of Double-Heterojunction Nanorod Light-Emitting Diodes. *Nanoscale* **2017**, *9*, 6103−6110.
(10) Nam, S.; Oh, N.; Zhai, Y.; Shim, M. High Efficiency and Optical Anisotropy in Double-Heterojunction Nanorod Light-Emitting Diodes. *ACS Nano* **2015**, *9*, 878−885.
(11) Oh, N.; Kim, B. H.; Cho, S.-Y.; Nam, S.; Rogers, S. P.; Jiang, Y.; Flanagan, J. C.; Zhai, Y.; Kim, J.-H.; Lee, J.; Yu, Y.; Cho, Y. K.; Hur, G.; Zhang, J.; Trefonas, P.; Rogers, J. A.; Shim, M. Double-Heterojunction Nanorod Light-Responsive LEDs for Display Applications. *Science* **2017**, *355*, 616−619.
(12) McDaniel, H.; Heil, P. E.; Tsai, C.-L.; Kim, K.; Shim, M. Integration of Type II Nanorod Heterostructures into Photovoltaics. *ACS Nano* **2011**, *5*, 7677−7683.
(13) Lee, S.; Flanagan, J. C.; Kang, J.; Kim, J.; Shim, M.; Park, B. Integration of CdSe/$CdSe_xTe_{1-x}$ Type-II Heterojunction Nanorods into Hierarchically Porous TiO_2 Electrode for Efficient Solar Energy Conversion. *Sci. Rep.* **2015**, *5*, 17472.
(14) Lee, S.; Flanagan, J. C.; Lee, B.; Hwang, T.; Kim, J.; Gil, B.; Shim, M.; Park, B. Route to Improving Photovoltaics Based on CdSe/$CdSe_xTe_{1-x}$ Type-II Heterojunction Nanorods: The Effect of Morphology and Cosensitization on Carrier Recombination and Transport. *ACS Appl. Mater. Interfaces* **2017**, *9*, 31931−31939.
(15) Sahasrabudhe, A.; Bhattacharyya, S. Dual Sensitization Strategy for High-Performance Core/Shell/Quasi-shell Quantum Dot Solar Cells. *Chem. Mater.* **2015**, *27*, 4848−4859.
(16) Luo, J.; Wei, H.; Huang, Q.; Hu, X.; Zhao, H.; Yu, R.; Li, D.; Luo, Y.; Meng, Q. Highly Efficient Core-Shell $CuInS_2$-Mn Doped CdS Quantum Dot Sensitized Solar Cells. *Chem. Commun.* **2013**, *49*, 3881−3883.
(17) Esparza, D.; Bustos-Ramirez, G.; Carriles, R.; López-Luke, T.; Zarazúa, I.; Martínez-Benítez, A.; Torres-Castro, A.; De la Rosa, E. Studying the Role of CdS on the TiO_2 Surface Passivation to Improve CdSeTe Quantum Dots Sensitized Solar Cell. *J. Alloys Compd.* **2017**, *728*, 1058−1064.
(18) Esparza, D.; Lopez-Luke, T.; Oliva, J.; Cerdán-Pasarán, A.; Martínez-Benítez, A.; Mora-Seró, I.; De la Rosa, E. Enhancement of Efficiency in Quantum Dot Sensitized Solar Cells Based on CdS/CdSe/CdSeTe Heterostructure by Improving the Light Absorption in the VIS-NIR Region. *Electrochim. Acta* **2017**, *247*, 899−909.
(19) McDaniel, H.; Oh, N.; Shim, M. CdSe-$CdSe_xTe_{1-x}$ Nanorod Heterostructures: Tuning Alloy Composition and Spatially Indirect Recombination Energies. *J. Mater. Chem.* **2012**, *22*, 11621−11628.
(20) Zhou, R.; Zhang, Q.; Tian, J.; Myers, D.; Yin, M.; Cao, G. Influence of Cationic Precursors on CdS Quantum-Dot-Sensitized Solar Cell Prepared by Successive Ionic Layer Adsorption and Reaction. *J. Phys. Chem. C* **2013**, *117*, 26948−26956.
(21) Sfaelou, S.; Sygellou, L.; Dracopoulos, V.; Travlos, A.; Lianos, P. Effect of the Nature of Cadmium Salts on the Effectiveness of CdS SILAR Deposition and its Consequence on the Performance of Sensitized Solar Cells. *J. Phys. Chem. C* **2014**, *118*, 22873−22880.
(22) Pernik, D. R.; Tvrdy, K.; Radich, J. G.; Kamat, P. V. Tracking the Adsorption and Electron Injection Rates of CdSe Quantum Dots on TiO_2: Linked versus Direct Attachment. *J. Phys. Chem. C* **2011**, *115*, 13511−13519.
(23) Lee, H. J.; Yum, J.-H.; Leventis, H. C.; Zakeeruddin, S. M.; Haque, S. A.; Chen, P.; Seok, S. I.; Grätzel, M.; Nazeeruddin, M. K. CdSe Quantum-Dot Sensitized Solar Cells Exceeding Efficiency 1% at Full-Sun Intensity. *J. Phys. Chem. C* **2008**, *112*, 11600−11608.
(24) Mora-Seró, I.; Giménez, S.; Moehl, T.; Fabregat-Santiago, F.; Lana-Villareal, T.; Gómez, R.; Bisquert, J. Factors Determining the Photovoltaic Performance of a CdSe Quantum Dot Sensitized Solar Cell: the Role of the Linker Molecule and of the Counter Electrode. *Nanotechnology* **2008**, *19*, 424007.
(25) Giménez, S.; Mora-Seró, I.; Macor, L.; Guijarro, N.; Lana-Villarreal, T.; Gómez, R.; Diguna, L. J.; Shen, Q.; Toyoda, T.; Bisquert, J. Improving the Performance of Colloidal Quantum-Dot-Sensitized Solar Cells. *Nanotechnology* **2009**, *20*, 295204.
(26) Esparza, D.; Zarazúa, I.; López-Luke, T.; Cerdán-Pasarán, A.; Sánchez-Solís, A.; Torres-Castro, A.; Mora-Sero, I.; De la Rosa, E. Effect of Different Sensitization Technique on the Photoconversion Efficiency of CdS Quantum Dot and CdSe Quantum Rod Sensitized TiO_2 Solar Cells. *J. Phys. Chem. C* **2015**, *119*, 13394−13403.
(27) Shen, Q.; Yamada, A.; Tamura, S.; Toyoda, T. CdSe Quantum Dot-Sensitized Solar Cell Employing TiO_2 Nanotube Working-Electrode and Cu_2S Counter-Electrode. *Appl. Phys. Lett.* **2010**, *97*, 123107.
(28) Hwang, T.; Lee, S.; Kim, J.; Kim, J.; Kim, C.; Shin, B.; Park, B. Tailoring the Mesoscopic TiO_2 Layer: Concomitant Parameters for Enabling High-Performance Perovskite Solar Cells. *Nanoscale Res. Lett.* **2017**, *12*, 57.
(29) Zhang, C.; Zhang, J.; Hao, Y.; Lin, Z.; Zhu, C. A Simple and Efficient Solar Cell Parameter Extraction Method from a Single Current-Voltage Curve. *J. Appl. Phys.* **2011**, *110*, 064504.
(30) Choi, H.; Hwang, T.; Lee, S.; Nam, S.; Kang, J.; Lee, B.; Park, B. The Construction of Tandem Dye-Sensitized Solar Cells from Chemically-Derived Nanoporous Photoelectrodes. *J. Power Sources* **2015**, *274*, 937−942.
(31) Nakamura, R.; Makuta, S.; Tachibana, Y. Electron Injection Dynamics at the SILAR Deposited CdS Quantum Dot/TiO_2 Interface. *J. Phys. Chem. C* **2015**, *119*, 20357−20362.
(32) Yang, J.; Wang, J.; Zhao, K.; Izuishi, T.; Li, Y.; Shen, Q.; Zhong, X. CdSeTe/CdS Type-I Core/Shell Quantum Dot Sensitized Solar Cells with Efficiency over 9%. *J. Phys. Chem. C* **2015**, *119*, 28800−28808.
(33) Yan, C.; Huang, J.; Sun, K.; Johnston, S.; Zhang, Y.; Sun, H.; Pu, A.; He, M.; Liu, F.; Eder, K.; Yang, L.; Cairney, J. M.; Ekins-Daukes, N. J.; Hameiri, Z.; Stride, J. A.; Chen, S.; Green, M. A.; Hao, X. Cu_2ZnSnS_4 Solar Cells with over 10% Power Conversion Efficiency Enabled by Heterojunction Heat Treatment. *Nat. Energy* **2018**, *3*, 764−772.
(34) Repins, I.; Contreras, M. A.; Egaas, B.; DeHart, C.; Scharf, J.; Perkins, C. L.; To, B.; Noufi, R. 19.9%-Efficient ZnO/CdS/$CuInGaSe_2$ Solar Cell with 81.2% Fill Factor. *Prog. Photovoltaics Res. Appl.* **2008**, *16*, 235−239.
(35) Leng, M.; Luo, M.; Chen, C.; Qin, S.; Chen, J.; Zhong, J.; Tang, J. Selenization of Sb_2Se_3 Absorber Layer: An Efficient Step to Improve Device Performance of CdS/Sb_2Se_3 Solar Cells. *Appl. Phys. Lett.* **2014**, *105*, 083905.
(36) Qiu, W.; Buffière, M.; Brammertz, G.; Paetzold, U. W.; Froyen, L.; Heremans, P.; Cheyns, D. High Efficiency Perovskite Solar Cells using a PCBM/ZnO Double Electron Transport Layer and a Short Air-Aging Step. *Org. Electron.* **2015**, *26*, 30−35.
(37) Fabregat-Santiago, F.; Garcia-Belmonte, G.; Mora-Seró, I.; Bisquert, J. Characterization of Nanostructured Hybrid and Organic Solar Cells by Impedance Spectroscopy. *Phys. Chem. Chem. Phys.* **2011**, *13*, 9083−9118.
(38) Bisquert, J.; Mora-Seró, I. Simulation of Steady-State Characteristics of Dye-Sensitized Solar Cells and the Interpretation of the Diffusion Length. *J. Phys. Chem. Lett.* **2010**, *1*, 450−456.
(39) González-Pedro, V.; Xu, X.; Mora-Seró, I.; Bisquert, J. Modeling High-Efficiency Quantum Dot Sensitized Solar Cells. *ACS Nano* **2010**, *4*, 5783−5790.
(40) O'Regan, B. C.; Durrant, J. R.; Sommeling, P. M.; Bakker, N. J. Influence of the $TiCl_4$ Treatment on Nanocrystalline TiO_2 Films in Dye-Sensitized Solar Cells. 2. Charge Density, Band Edge Shifts, and Quantification of Recombination Losses at Short Circuit. *J. Phys. Chem. C* **2007**, *111*, 14001−14010.
(41) Seger, B.; Tilley, S. D.; Pedersen, T.; Vesborg, P. C. K.; Hansen, O.; Grätzel, M.; Chorkendorff, I. Silicon Protected with Atomic Layer Deposited TiO_2: Conducting *versus* Tunnelling through TiO_2. *J. Mater. Chem. A* **2013**, *1*, 15089−15094.
(42) Evangelista, R. M.; Makuta, S.; Yonezu, S.; Andrews, J.; Tachibana, Y. Semiconductor Quantum Dot Sensitized Solar Cells Based on Ferricyanide/Ferrocyanide Redox Electrolyte Reaching an Open Circuit Photovoltage of 0.8 V. *ACS Appl. Mater. Interfaces* **2016**, *8*, 13957−13965.

DOI: 10.1021/acsami.9b02873
ACS Appl. Mater. Interfaces XXXX, XXX, XXX−XXX

(43) Sambur, J. B.; Novet, T.; Parkinson, B. A. Multiple Exciton Collection in a Sensitized Photovoltaic System. *Science* **2010**, *330*, 63−66.
(44) Chi, C.-F.; Cho, H.-W.; Teng, H.; Chuang, C.-Y.; Chang, Y.-M.; Hsu, Y.-J.; Lee, Y.-L. Energy Level Alignment, Electron Injection, and Charge Recombination Characteristics in CdS/CdSe Cosensitized TiO_2 Photoelectrode. *Appl. Phys. Lett.* **2011**, *98*, 012101.
(45) Lee, Y.-L.; Lo, Y.-S. Highly Efficient Quantum-Dot-Sensitized Solar Cell Based on Co-Sensitization of CdS/CdSe. *Adv. Funct. Mater.* **2009**, *19*, 604−609.
(46) Pan, Z.; Zhang, H.; Cheng, K.; Hou, Y.; Hua, J.; Zhong, X. Highly Efficient Inverted Type-I CdS/CdSe Core/Shell Structure QD-Sensitized Solar Cells. *ACS Nano* **2012**, *6*, 3982−3991.
(47) Itzhakov, S.; Shen, H.; Buhbut, S.; Lin, H.; Oron, D. Type-II Quantum-Dot-Sensitized Solar Cell Spanning the Visible and Near-Infrared Spectrum. *J. Phys. Chem. C* **2013**, *117*, 22203−22210.
(48) Wang, J.; Mora-Seró, I.; Pan, Z.; Zhao, K.; Zhang, H.; Feng, Y.; Yang, G.; Zhong, X.; Bisquert, J. Core/Shell Colloidal Quantum Dot Exciplex States for the Development of Highly Efficient Quantum-Dot-Sensitized Solar Cells. *J. Am. Chem. Soc.* **2013**, *135*, 15913−15922.
(49) Jiao, S.; Shen, Q.; Mora-Seró, I.; Wang, J.; Pan, Z.; Zhao, K.; Kuga, Y.; Zhong, X.; Bisquert, J. Band Engineering in Core/Shell ZnTe/CdSe for Photovoltage and Efficiency Enhancement in Exciplex Quantum Dot Sensitized Solar Cells. *ACS Nano* **2015**, *9*, 908−915.
(50) Pan, Z.; Mora-Seró, I.; Shen, Q.; Zhang, H.; Li, Y.; Zhao, K.; Wang, J.; Zhong, X.; Bisquert, J. High-Efficiency "Green" Quantum Dot Solar Cells. *J. Am. Chem. Soc.* **2014**, *136*, 9203−9210.
(51) Luo, S.; Kazes, M.; Lin, H.; Oron, D. Strain-Induced Type II Band Alignment Control in CdSe Nanoplatelet/ZnS-Sensitized Solar Cells. *J. Phys. Chem. C* **2017**, *121*, 11136−11143.
(52) Kim, B.; Kim, K.; Kwon, Y.; Lee, W.; Shin, W. H.; Kim, S.; Bang, J. $CuInS_2$/CdS-Heterostructured Nanotetrapods by Seeded Growth and Their Photovoltaic Properties. *ACS Appl. Nano Mater.* **2018**, *1*, 2449−2454.
(53) Zhao, K.; Pan, Z.; Mora-Seró, I.; Cánovas, E.; Wang, H.; Song, Y.; Gong, X.; Wang, J.; Bonn, M.; Bisquert, J.; Zhong, X. Boosting Power Conversion Efficiencies of Quantum-Dot-Sensitized Solar Cells Beyond 8% by Recombination Control. *J. Am. Chem. Soc.* **2015**, *137*, 5602−5609.
(54) Ren, Z.; Wang, J.; Pan, Z.; Zhao, K.; Zhang, H.; Li, Y.; Zhao, Y.; Mora-Sero, I.; Bisquert, J.; Zhong, X. Amorphous TiO_2 Buffer Layer Boosts Efficiency of Quantum Dot Sensitized Solar Cells to over 9%. *Chem. Mater.* **2015**, *27*, 8398−8405.
(55) Yu, J.; Wang, W.; Pan, Z.; Du, J.; Ren, Z.; Xue, W.; Zhong, X. Quantum Dot Sensitized Solar Cells with Efficiency over 12% Based on Tetraethyl Orthosilicate Additive in Polysulfide Electrolyte. *J. Mater. Chem. A* **2017**, *5*, 14124−14133.
(56) Jiao, S.; Du, J.; Du, Z.; Long, D.; Jiang, W.; Pan, Z.; Li, Y.; Zhong, X. Nitrogen-Doped Mesoporous Carbons as Counter Electrodes in Quantum Dot Sensitized Solar Cells with a Conversion Efficiency Exceeding 12%. *J. Phys. Chem. Lett.* **2017**, *8*, 559−564.
(57) Pan, Z.; Rao, H.; Mora-Seró, I.; Bisquert, J.; Zhong, X. Quantum Dot-Sensitized Solar Cells. *Chem. Soc. Rev.* **2018**, *47*, 7659−7702.

DOI: 10.1021/acsami.9b02873
ACS Appl. Mater. Interfaces XXXX, XXX, XXX−XXX